

Gyrokinetic simulation of turbulence under lower hybrid wave and electron cyclotron wave combined heating on EAST

Zhengyao Xiao¹, Xinxia Li^{1,†}, Qi Zhong² and Miaohui Li³

¹School of Nuclear Science and Technology, University of South China, Hengyang 421001, PR China

²Institute for Fusion Theory and Simulation, Zhejiang University, Hangzhou 310027, PR China

³Institute of Plasma Physics, Chinese Academy of Sciences, Hefei 230031, PR China

(Received 28 January 2024; revised 28 June 2024; accepted 1 July 2024)

On the Experimental Advanced Superconducting Tokamak (EAST), the electron cyclotron wave (ECW) and lower hybrid wave (LHW) are actively used to achieve a high-performance plasma. Turbulence associated with the combined heating experiment is studied numerically based on the gyrokinetic toroidal code (GTC). The linear simulation results show that the unstable mode peaks at $k_{\theta}\rho_s \approx 0.65$ and $k_{\theta}\rho_s \approx 1.42$. Meanwhile, all of the frequencies of these instabilities are positive, which suggests that the collisionless trapped electron mode (CTEM) is the dominant instability. In the process of nonlinear simulations, a higher transport level is locally achieved during the two waves combined heating due to a formation of a steeper electron temperature gradient. In addition, a low-frequency geodesic acoustic mode (GAM) is observed in the nonlinear stage. Effects of the electron beta, the dimensionless ratio of T_e/T_i and R/L_{T_e} on the growth rate of instability, are also discussed in the paper.

Key words: plasma instabilities, plasma simulation, plasma nonlinear phenomena

1. Introduction

Radio frequency (RF) wave heating and current drive play a crucial role in achieving steady-state operation of a tokamak. It is generally found that the plasma transport level during the transition to high confinement mode (H-mode) via RF heating is much higher than the prediction by neoclassical transport theory. This anomalous transport primarily arises from the drift wave instabilities in plasmas (Diamond *et al.* 2005). Among them, the ion temperature gradient (ITG) mode, trapped electron mode (TEM) and electron temperature gradient (ETG) mode are the most important candidates (Horton 1999; Ryter *et al.* 2005; Bonanomi *et al.* 2015). Although the ion turbulent transport driven by the ITG turbulence is well understood, understanding of the electron turbulent transport remains inadequate due to the complex kinetic mechanisms involved (Xiao *et al.* 2010). To achieve better performance for a tokamak operation scenario, several plasma heating and current

† Email address for correspondence: li_xx@usc.edu.cn

drive methods are applied simultaneously in tokamaks, and positive synergistic effects of current drive are generally observed (Fidone *et al.* 1987; Dumont & Giruzzi 2004; Giruzzi *et al.* 2004). However, less work has been done on the turbulent transport during these combined heating processes, where a much steeper temperature profile is usually formed, which can affect the turbulence transport level in turn.

A complete understanding of the plasma turbulent transport is crucial in the operations of tokamaks. Gyrokinetic simulation offers valuable insights into turbulent transport driven by drift waves. Recent experiments at ASDEX Upgrade in H-mode have demonstrated through gyrokinetic simulations that the ITG mode contributes predominantly to ion heat transport, while also contributing partially to electron heat transport (Ryter *et al.* 2019). In scenarios with high poloidal plasma beta β_p and internal transport barriers (ITB) in EAST, the drift instabilities persist particularly for lower q_{95} values (<7.0). Various types of instabilities, including ITG, TEM and ETG, manifest their existence in different radial regions of tokamak plasmas (Ding *et al.* 2019). Notably, advancements in electron modelling based on gyrokinetic theory have been developed, with integration into simulation codes such as GTC, GT3D and FULL (Lin *et al.* 2007; Rewoldt, Lin & Idomura 2007), allowing for a deeper investigation into the electron effects on turbulence.

In this work, the turbulence in the present EAST plasma under lower hybrid wave (LHW) and electron cyclotron wave (ECW) combined heating is studied numerically using the GTC code where the kinetic electrons are retained. The remaining sections of the paper are organized as follows. In § 2, the experimental performances associated with the combined heating are introduced for EAST tokamak plasmas. The simulation model and the related plasma parameter settings are described in § 3. In § 4, both the linear and nonlinear simulation results are presented. Parametric scans of the electron beta, the dimensionless ratio of T_e/T_i and R/L_{Te} , are carried out and their effects on the electrostatic drift wave instability are also shown. Turbulent transport and zonal flow physics are investigated for the combined heating cases. Finally, a discussion and conclusions are provided in § 5.

2. Experimental set-up

EAST, a fully superconducting tokamak with a non-circular cross-section, has a major radius $R = 1.9$ m and a minor radius $a = 0.4$ m. Through continuous improvement in auxiliary heating systems, the 2022 campaign witnessed the attainment of H-mode plasmas sustained for a record of approximately 310 s. Notably, both ECW and LHW systems play crucial roles as the primary sources for electron heating and current drive, enabling EAST's long-pulse operations. Figure 1 illustrates a typical deuterium plasma discharge, as seen in EAST shot #98933, characterized by a toroidal magnetic field $B_T = 2.4$ T, a plasma current I_p of 518 kA, a line-averaged electron density of $n_e = 1.7 \times 10^{19} \text{ m}^{-3}$ and nearly zero loop voltage sustained throughout the discharge.

During the discharge of EAST shot #98933, both LHW at 2.3 MW and 4.6 GHz, and ECW at 1.4 MW and 10 GHz were injected into the plasma starting from 1.7 s. However, the ECW power was temporarily shut down from 38 to 56 s. Another EAST shot #98958, exhibited similar discharge parameters to shot #98933, except that the ECW remained active throughout the entire discharge. In this study, shot #98933 at 50.3 s will be referred to as the LHW-only case and shot #98958 at 10.0 s will be referred to as the LHW+ECW case or the combined heating case. Figure 2 displays the radial profiles for electron temperature measured by Thomson scattering (TS) and of ion temperature measured by an X-ray crystal spectrometer (XCS). The data clearly indicate a decrease in peak electron temperature from 13 to 6.5 keV when the ECW system was deactivated.

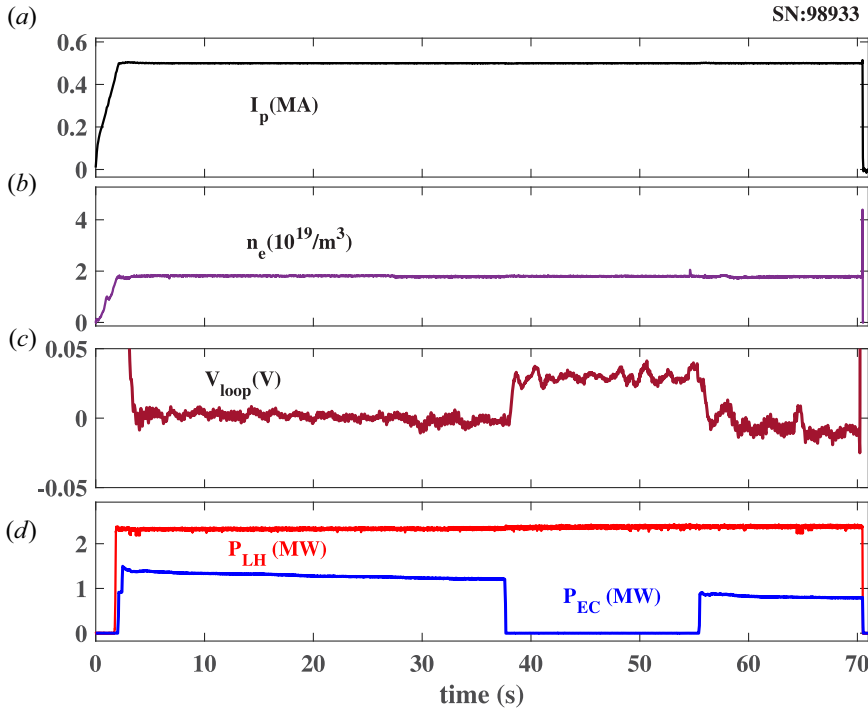


FIGURE 1. Time traces of EAST discharge carried out with LHW and ECW. (a) Plasma current, (b) line-averaged electron density, (c) loop voltage and (d) heating powers of LHW and ECW.

Magnetic equilibrium was determined using the EFIT equilibrium code, while electron density measurements were obtained via TS and reflectometry. The safety factor q profile was derived by incorporating Faraday rotation measurements from a polarimeter and interferometer measurement as additional constraints in the EFIT code (Lao *et al.* 1985; Wang *et al.* 2013; Qian *et al.* 2016).

3. Simulation model and set-up

The GTC code is a three-dimensional global gyrokinetic particle code that uses Boozer coordinates to handle realistic magnetic field geometry (Zhao & Xiao 2018). Given that drift wave turbulence predominantly occurs on the ion gyro-radius scale, the GTC code employs gyrokinetics for ions and drift kinetics for electrons. The perturbation part of the ion distribution function $\delta f \approx f_i - f_{Mi}$ satisfies the following gyrokinetic equation (Hahn 1988; Lin *et al.* 2007):

$$\begin{aligned} \frac{d\delta f_i}{dt} &\equiv \left[\frac{\partial}{\partial t} + (v_{\parallel} \mathbf{b} + \mathbf{v}_d + \langle \mathbf{v}_E \rangle_{\varphi}) \cdot \nabla - \mathbf{b}^* \cdot \nabla \left(\mu B + Z_i e \langle \phi \rangle_{\varphi} \frac{\partial}{m_i \partial v_{\parallel}} \right) \right] \delta f_i \\ &= -f_i \left(\langle \mathbf{v}_E \rangle_{\varphi} \cdot \nabla \ln f_{Mi} - \mathbf{b}^* \cdot \nabla \langle \phi \rangle_{\varphi} \frac{Z_i e \partial}{m_i \partial v_{\parallel}} \ln f_{Mi} \right), \end{aligned} \quad (3.1)$$

where v_{\parallel} is the parallel velocity for the particle and $\mu = mv_{\perp}^2/2B$ denotes its magnetic moment. In this equation, $\mathbf{b}^* = \mathbf{b} + (m_i c / (Z_i e B)) v_{\parallel} \nabla \times \mathbf{b}$, $\langle \mathbf{v}_E \rangle_{\varphi} = c \mathbf{b} \times \nabla \langle \phi \rangle_{\varphi} / B$ with $\langle \phi \rangle_{\varphi} = (1/2\pi) \int \phi(\mathbf{x}) \delta(\mathbf{x} - \mathbf{R} - \rho) d\mathbf{x} d\varphi$ as the gyroaveraged electrostatic potential, $\mathbf{v}_d = \mathbf{v}_c + \mathbf{v}_g$ with $\mathbf{v}_c = (v_{\parallel} / \Omega_i) \nabla \times \mathbf{b}$ and $\mathbf{v}_g = (\mu / m_i \Omega_i) \mathbf{b} \times \nabla B$. The electron distribution function obeys $f_e \approx f_{Me} + (e \delta \phi / T_e) f_{Me} + \delta g_e$ with $e \delta \phi / T_e \ll 1$ and satisfies

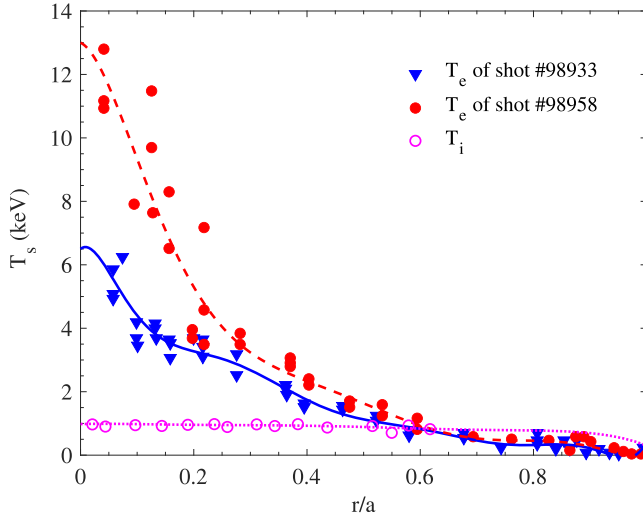


FIGURE 2. Electron and ion temperature radial profiles with ECW (EAST shot #98958) and without ECW (EAST shot #98933).

the drift kinetic equation (Lin *et al.* 2007):

$$\begin{aligned}
 & \left[\frac{\partial}{\partial t} + (\mathbf{v}_{\parallel} + \mathbf{v}_d + \mathbf{v}_E) \cdot \nabla - \mathbf{b}^* \cdot \nabla (\mu B - e\phi) \frac{\partial}{m_e \partial v_{\parallel}} \right] \delta g_e \\
 & = -f_{Me} \exp\left(\frac{e\delta\phi}{T_e}\right) \left(\frac{\partial}{\partial t} \left(\frac{e\delta\phi}{T_e} \right) + \delta \mathbf{v}_E \cdot \nabla \ln f_{Me} \right) \\
 & - (\mathbf{v}_d + \delta \mathbf{v}_E) \cdot \nabla \left(\frac{e\langle\phi\rangle}{T_e} \right), \tag{3.2}
 \end{aligned}$$

where $\delta \mathbf{v}_E = (c\mathbf{b} \times \nabla \langle\delta\phi\rangle_{\varphi})/B$. Following the electrostatic assumption, the gyrokinetic Poisson equation is used to calculate the electric potential ϕ :

$$\frac{Z_i^2 e n_{i0}}{T_i} \phi - \frac{Z_i^2 e n_{i0}}{T_i} \tilde{\phi} = Z_i \bar{n}_i - \delta n_e^{(1)}, \tag{3.3}$$

with $\bar{n}_i = \int \delta(\mathbf{x} - \mathbf{R} - \boldsymbol{\rho}) \delta f_i d\mathbf{R} d^3v$ and $\delta n_e^{(1)} = \int \delta(\mathbf{x} - \mathbf{R} - \boldsymbol{\rho}) \delta g_e d\mathbf{R} d^3v$. In the equation, $\tilde{\phi}$ is the second-order gyro-averaged potential as

$$\tilde{\phi} = \frac{1}{2\pi} \int \delta\langle\phi\rangle_{\varphi}(R) \delta(\mathbf{x} - \mathbf{R} - \boldsymbol{\rho}) F_{Mi}(R, \mu, v_{\parallel}) d\mathbf{R} d^3v. \tag{3.4}$$

Taking a flux surface average on both sides of (3.3), the zonal flow equation is can be obtained. Divide the perturbation potential into two parts, i.e. $\phi = \delta\phi + \langle\phi\rangle$, where $\delta\phi$ is the non-zonal flow part and $\langle\phi\rangle$ is the zonal flow part. The zonal flow part can be calculated by the following zonal flow equation:

$$\langle \nabla_{\perp}^2 \phi \rangle = \left\langle - \left(\frac{T_i}{Z_i^2 n_i \rho_i^2} - \frac{T_i}{Z_i^2 n_2} \nabla_{\perp}^2 \right) (Z_i \delta \bar{n}_i - \delta n_e^{(1)}) \right\rangle. \tag{3.5}$$

In the equation, Z_i is the ion charged number, n is the density and ρ_i is the ion gyroradius. In the code, a nonlinear δf method is employed to simulate the complex nonlinear turbulence

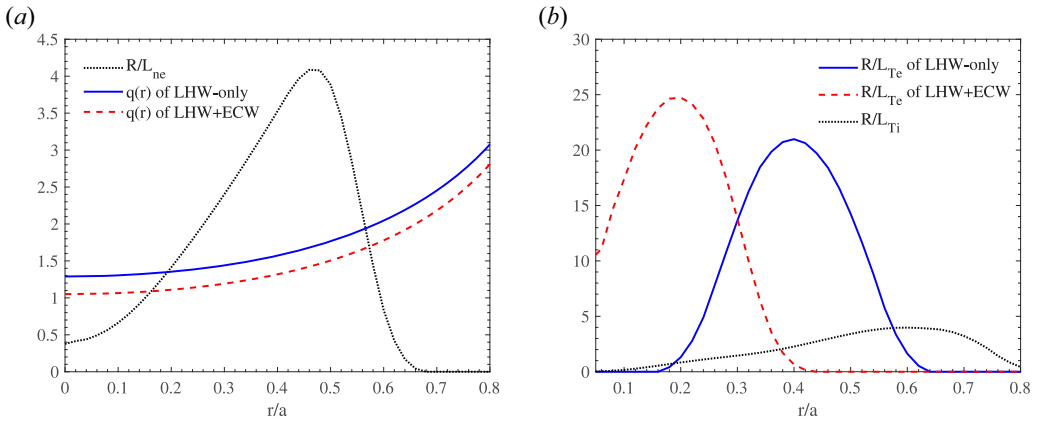


FIGURE 3. (a) Radial profiles of $q(r)$, gradient of plasma density and (b) gradient of plasma temperature.

Shots	r/a	R/L_{Te}	R/L_{Ti}	R/L_n	T_e/T_i	q	s	T_e (keV)	β_e
#98933(LHW-only)	0.40	20.5	2.2	3.3	1.99	1.57	0.41	1.77	0.29 %
#98958(LHW+ECW)	0.22	24.4	1.0	1.4	5.25	1.12	0.14	4.98	0.92 %

TABLE 1. Parameters of diagnostic points of two cases.

physics with relatively low particle noise (Dimitis & Lee 1993; Lin, Tang & Lee 1995) and the kinetic electron response is retained in the simulation.

The electrostatic drift wave instabilities in tokamak plasmas are generally believed to be driven by plasma pressure gradients. The GTC code assumes a zero radial boundary condition for the global simulation. To eliminate the boundary effect, numerical flattening and smoothing are employed to reduce turbulence drive close to both boundaries (Xiao *et al.* 2015).

Figure 3 displays the profiles of $q(r)$, density gradient scale length (R/L_n) and radial temperature gradient scale length ($R/L_{T\alpha}$, $\alpha = i, e$) associated with the aforementioned shots. The data range from $r/a = 0.1$ to $r/a = 0.4$ for the LHW-only case and $r/a = 0.28$ to $r/a = 0.57$ for the LHW+ECW case correspond to the experimental profiles, while the remaining range is smoothed out artificially. Given the negligible change in the ion temperature profile during these discharges, a fixed ion temperature profile is adopted in this study. In figure 3, it is evident that the maximum R/L_{Te} significantly exceeds R/L_{Ti} and R/L_n along radial positions, where $L_T = -(d \ln T/dr)^{-1}$ and $L_n = -(d \ln n/dr)^{-1}$. Table 1 lists several essential parameters at two radial diagnostic points used for the simulation, i.e. $r/a = 0.40$ and $r/a = 0.22$, where β_e denotes the electron plasma beta with $\beta_e = 8\pi n_e T_e / B^2$ and s represents the magnetic shear.

After conducting many numerical convergence tests, the radial grid number is set as $N_r = 100$ and poloidal grid number is set as $N_\theta = 1000$ for the LHW-only case. For the LHW+ECW case, a radial grid number of 120 and a poloidal grid number of 800 have been chosen to ensure the convergence criterion is met. The time step $t_0 = 0.02R_0/c_s$ is deemed sufficient for our simulations, where the ion sound speed $c_s = \sqrt{T_e/m_i}$.

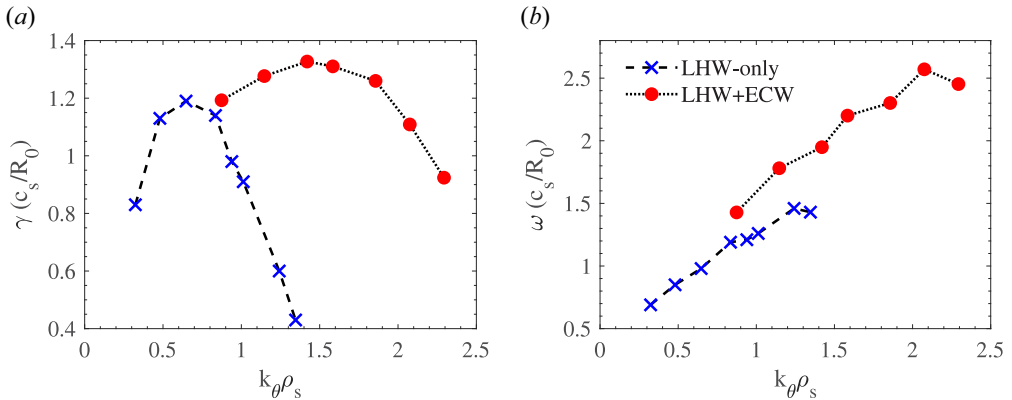


FIGURE 4. Linear dispersion relations of electrostatic instability for shot #98933 (LHW-only) and #98958 (LHW+ECW). (a) Linear growth rate, (b) real frequency.

4. Simulation results

4.1. Linear simulation results

Preliminary simulation results indicate that the instability arises solely when kinetic electrons are taken into account. To enhance the numerical accuracy of the dispersion relation within the code, we implement a filtering method. This method involves selecting a specific toroidal mode n at the diagnostic point, followed by selecting a set of poloidal modes m based on the safety factor $q = m/n$. The dispersion relations are depicted in figure 4, where k_θ represents the poloidal wave vector. To quantitatively compare the growth rate of the two cases, both c_s and ρ_s are taken from the simulation results of the LHW-only case. As illustrated in the figure, the real frequency of the instability is intensified in the LHW-only case, along with an increase in $k_\theta \rho_s$. Additionally, all real frequencies are shown to be positive, implying the dominance of the collisionless trapped electron mode (CTEM), which propagates in the electron diamagnetic direction. Furthermore, the broadening of the growth rate spectrum in the LHW+ECW case suggests the possibility of more CTEMs with shorter wavelengths. On one hand, for the LHW-only case, the most unstable mode occurs at $k_\theta \rho_s \approx 0.65$ with a growth rate of $1.19c_s/R_0$, which may decrease to $1.12c_s/R_0$ at the same wavelength for the LHW+ECW case. On the other hand, in the LHW+ECW case, the most unstable mode appears at $k_\theta \rho_s \approx 1.42$ with a growth rate of $1.33c_s/R_0$.

To investigate more about the linear dispersion physics as shown in figure 4, we conduct scans of several critical parameters, the results of which are presented in figure 5. Our analysis primarily focuses on the LHW-only case, specifically considering the most unstable mode $k_\theta \rho_s \approx 0.65$. In figure 5, it is evident that the instability is amplified with increasing R/L_{Te} , while an obvious decrease occurs with higher β_e and T_e/T_i . This observation suggests that the growth rate of the mode increases with increasing R/L_{Te} , which accords with the physical description of CTEM. Since the electron temperature at the diagnostic point is fixed, so the ion diamagnetic velocity diminishes with increasing T_e/T_i . In our simulation, the electron temperature remains constant; hence, a relatively larger β_e corresponds to higher plasma density, elevating the trapped electron and ion density, and consequently increasing the growth rate. However, β_e values exceeding 0.6% have resulted in a decrease in the growth rate, potentially due to the stabilizing effect of finite plasma pressure on drift wave instabilities (Dong, Chen & Zonca 1999). This implies

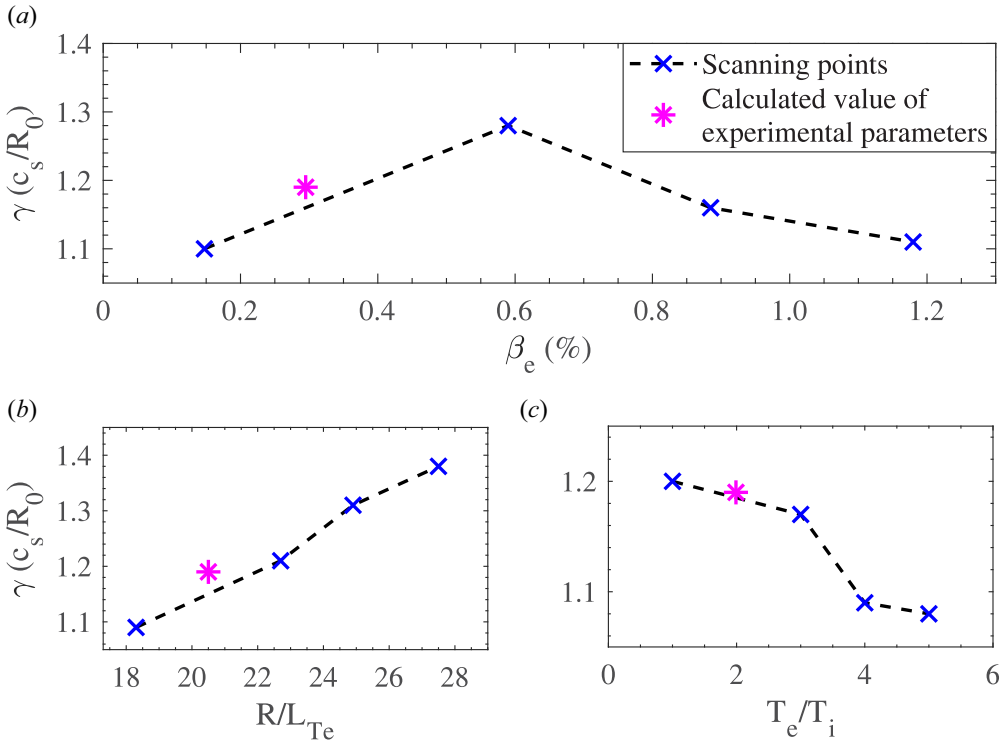


FIGURE 5. Dependence of the linear growth rate for $k_\theta \rho_s = 0.65$ on the following parameters: (a) β_e ; (b) electron temperature gradient scale length R/L_{T_e} and (c) T_e/T_i .

that R/L_{T_e} serves as the primary factor influencing the discrepancy in growth rates of the most unstable modes.

The two-dimensional poloidal mode structures for different $k_\theta \rho_s$ are plotted in figure 6 for the electrostatic potential at $t = 1800t_0$, corresponding to $k_\theta \rho_s \sim 0.65$, $k_\theta \rho_s \sim 0.94$, $k_\theta \rho_s \sim 1.24$ in the LHW-only case and $k_\theta \rho_s \sim 1.15$, $k_\theta \rho_s \sim 1.58$, $k_\theta \rho_s \sim 2.08$ in the LHW+ECW case. A conventional ballooning mode structure, peaking at the outer mid-plane, is observed. Additionally, the width of the mode structure gradually narrows as $k_\theta \rho_s$ increases. These results align well with ballooning-mode theory, where the width of the mode structure is proportional to k_θ^{-2} and the mode amplitude factor A is proportional to $n^{-1/2}$ (Hahn, Wang & Madsen 2009; Dickinson *et al.* 2014).

4.2. Nonlinear simulation results

Following the excitation of electrostatic instability, the zonal flow is triggered through nonlinear mode coupling among various high- n drift modes. Zonal flow typically serves as the primary saturation mechanism for ITG turbulence (Lin *et al.* 1998; Xiao *et al.* 2010). However, there remains a lack of definitive theory and consensus regarding the impact of zonal flow on TEM turbulence (Lang, Chen & Parker 2007). Consequently, simulations are conducted with both artificially removed and self-consistently generated zonal flows to explore the zonal flow effect on the EAST plasma turbulence. Figure 7 illustrates time evolutions of turbulent heat diffusivity for both cases from the GTC simulation. The ion heat diffusivity χ_i can be calculated by the relationship $q_j = n_j \chi_j \nabla T_j$. Heat flux q_j is calculated in the simulation by $q_j = \int dv^3 (m_j v^2 / 2 - 3T_j / 2) \delta v_E \delta f_j$, where v_E represents the

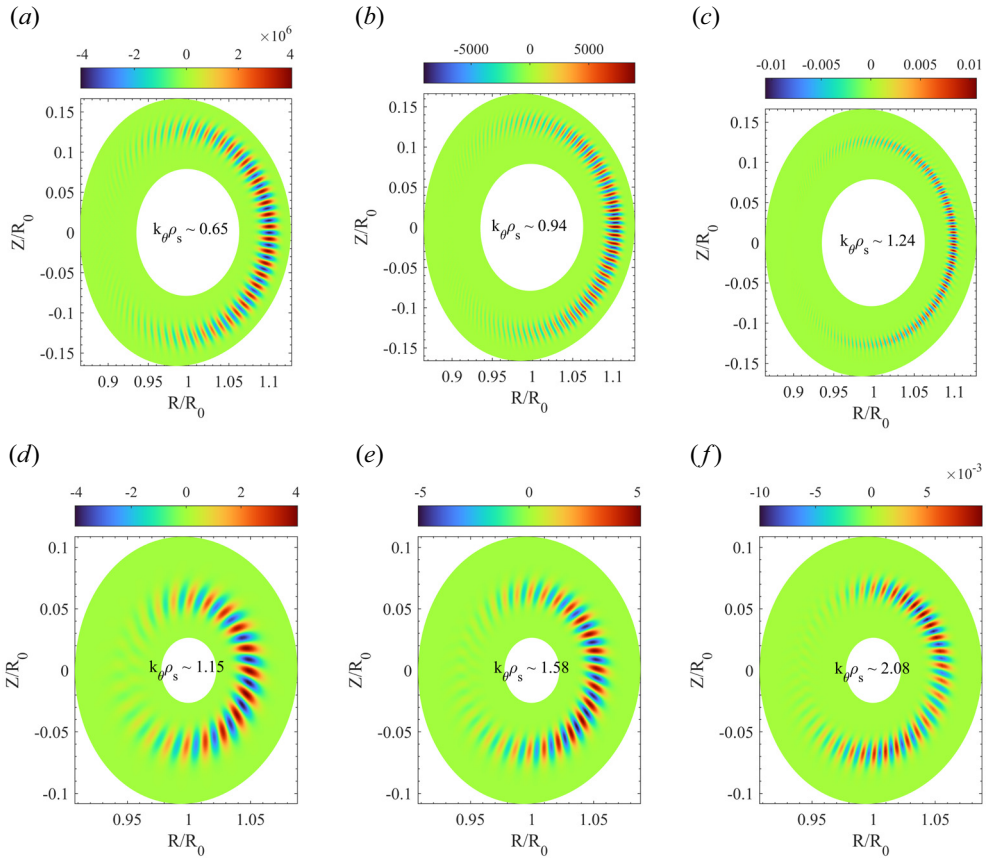


FIGURE 6. Poloidal structures of electrostatic potential (*a–c*) for the LHW-only case and (*d–f*) for the LHW+ECW case.

$E \times B$ drift induced by the turbulent fluctuations (Xie, Xiao & Lin 2017). It is evident from the figure that ion heat diffusivity significantly surpasses that of electrons in both cases during the nonlinear saturation phase of turbulence, which suggests the predominance of ion transport for this parameter setting. Interestingly, a similar phenomenon is also observed in EAST plasma during high β_p discharge (Zheng *et al.* 2022). Table 2 provides a quantitative comparison of particle heat diffusivities, revealing lower heat diffusivity when the zonal flow is preserved. For the LHW-only heating, ion heat diffusivity is reduced by 66% by comparing cases with and without zonal flow, while for the LHW+ECW combined heating, it is reduced by 59%. Moreover, the time-averaged ion heat diffusivity for the LHW+ECW case is approximately 52% higher than that in the LHW-only case when the zonal flow is retained. This result indicates that the transport level of the LHW+ECW case exceeds that of the LHW-only case, attributed to the significantly higher growth rate of instability observed in the LHW+ECW case.

Figure 8 illustrates the poloidal structures of turbulent electrostatic potential during the nonlinear saturation phases. It is evident from the figure that the electrostatic potentials in the outer mid-plane, where bad curvature occurs, are notably higher than those in the inner mid-plane, where good curvature occurs. Radial turbulent eddies with elongated structures are observed in figure 8(*a,c*). The intensity of turbulence transport decreases significantly as the radial elongated structures are destroyed in figure 8(*b,d*). This suggests that the shear

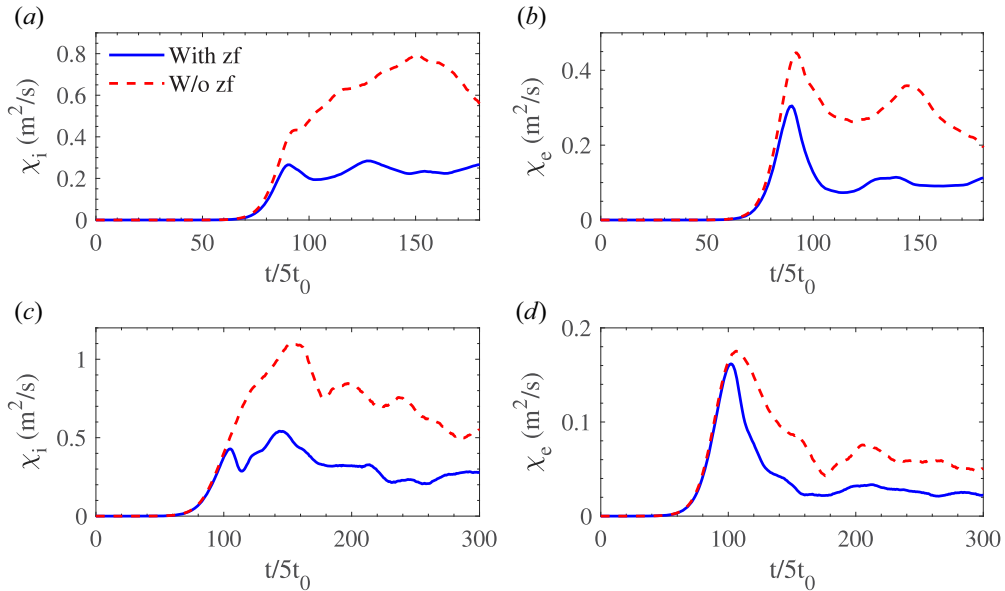


FIGURE 7. Time evolutions of particles heat diffusivity χ_s (a,b) for the LHW-only case and (c,d) for the LHW+ECW case with zonal flow or removed in the nonlinear simulation.

Cases	χ_i ($\text{m}^2 \text{s}^{-1}$)	χ_e ($\text{m}^2 \text{s}^{-1}$)
LHW-only w/o zonal	0.68	0.30
LHW-only with zonal	0.23	0.09
LHW+ECW w/o zonal	0.85	0.07
LHW+ECW with zonal	0.35	0.03

TABLE 2. Time average ion and electron heat diffusivities in different cases with or without zonal flow.

effect of zonal flow contributes to the reduction of radial correlation length and thereby suppresses turbulent transport.

However, [table 2](#) clearly shows that the time-averaged electron heat diffusivity is decreased by 57 % for the LHW+ECW combined heating case when the zonal flow is retained, which is 70 % for the LHW-only heating case. This finding suggests that the zonal flow does not exert the same regulation effect on electron heat transport for the two cases, which may be influenced by parameters such as R/L_{Te} and T_e/T_i in the CTEM turbulence (Lang, Parker & Chen 2008). Conversely, a significant oscillation in ion heat diffusivity occurs in the LHW-only case during the turbulent saturation period when the zonal flow is retained. According to the theory of zonal flow dynamics, a low-frequency GAM during turbulent saturation stage typically manifests as an oscillation (Diamond *et al.* 2005), suggesting the potential existence of a GAM in the simulation.

The time history of the radial structure of the electric field E_r associated with the zonal flow is shown in [figure 9](#). Oscillations of E_r are clearly observed in [figure 9\(a\)](#), indicating the presence of GAMs for the LHW-only heating case. Based on time evolution of GAM/ZF intensity at the reference radius in [figure 10](#), the real frequency of the

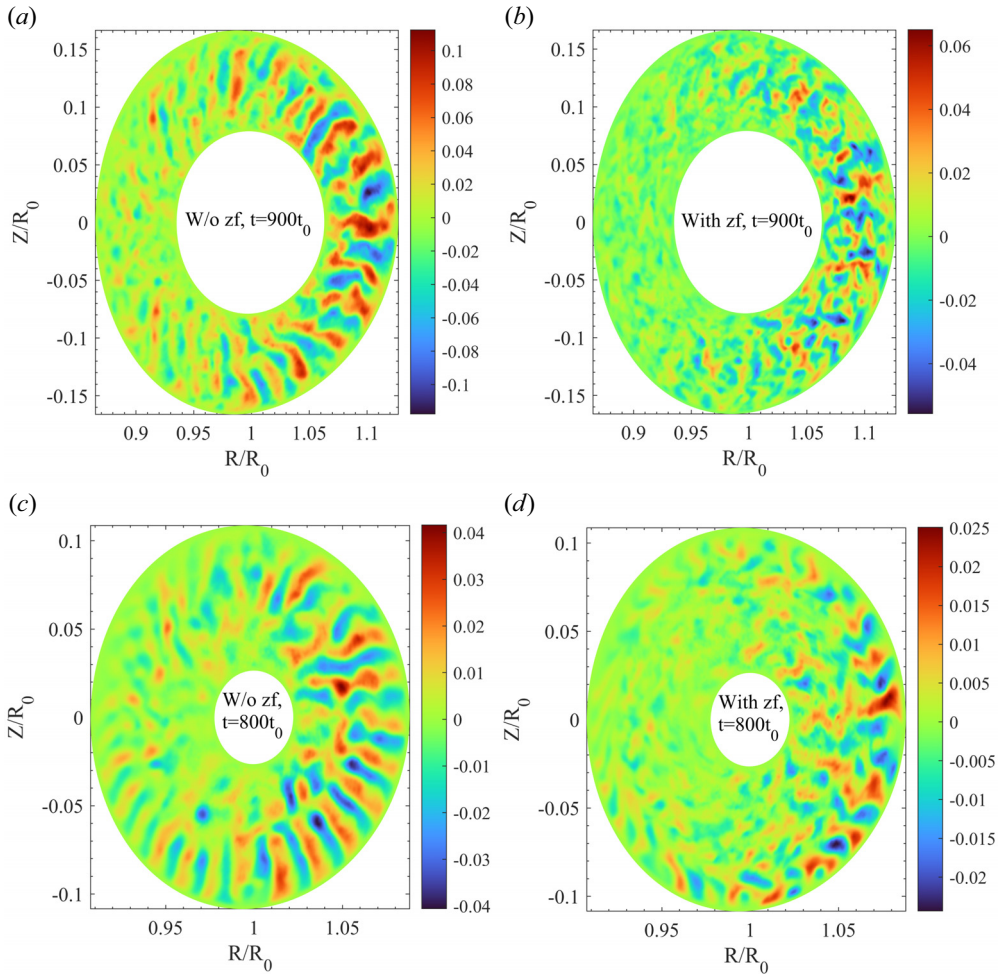


FIGURE 8. Poloidal mode structures of turbulence electrostatic potential (a,b) for the LHW-only case and (c,d) for the LHW+ECW case.

oscillation can be approximately calculated. In fact, we obtain $\omega_{\text{LHW-only}}^{\text{simulation}} = 1.25c_s/R_0$, which is very close to theoretical prediction of tokamak magnetic configuration correction (Gao *et al.* 2006; Gao 2010), i.e. $\omega_{\text{LHW-only}}^{\text{theory}} = 1.30c_s/R_0$. However, in the LHW+ECW case, the turbulent field does not excite GAM, which may be due to stronger GAM damping in the lower q region and the method that uses a uniform marker particle temperature in the simulation.

5. Conclusion

The current EAST experiment, using combined heating from LHW and ECW, has demonstrated a notable effect on turbulent transport. In this study, gyrokinetic simulations employing the GTC code were conducted to investigate electrostatic drift wave instabilities and turbulence in EAST plasmas with the heating process of combining LHW and ECW. Our findings reveal that turbulent transport is locally heightened due to the steeper electron temperature gradient in the core plasma induced by LHW+ECW combined heating. Linear simulation results suggest that the CTEM is the dominant instability for both heating cases,

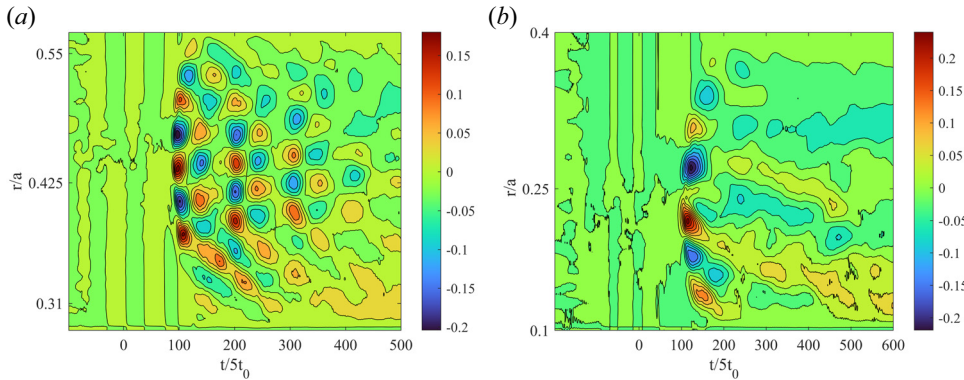


FIGURE 9. Two-dimensional time and radial mode structure of zonal flow for electric field E_r (a) in the LHW-only case and (b) in the LHW+ECW case.

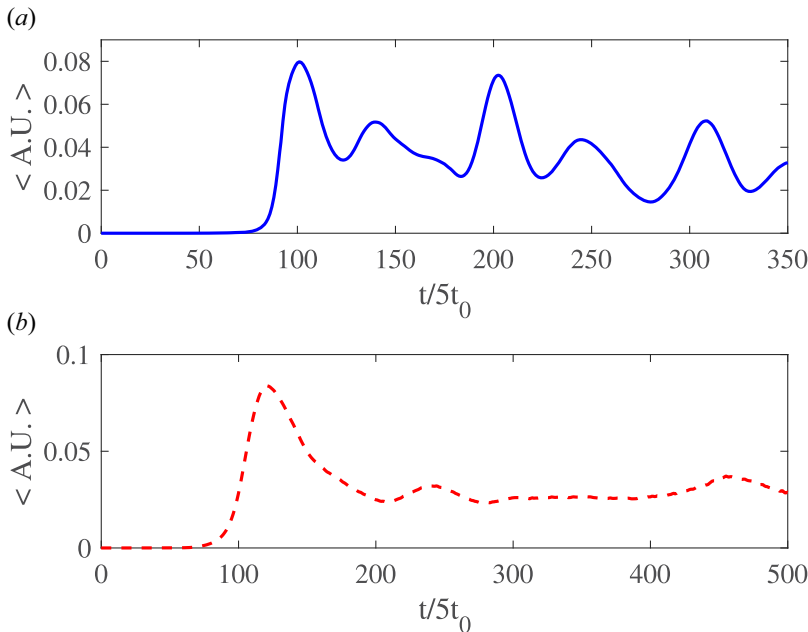


FIGURE 10. Time evolution of GAM/ZF intensity at the reference magnetic surface (a) in the LHW-only case and (b) in the LHW+ECW case.

with the most unstable modes occurring at $k_\theta \rho_s \approx 0.65$ and $k_\theta \rho_s \approx 1.42$ for the LHW-only case and LHW+ECW case, respectively. Furthermore, a higher ratio of T_e/T_i is shown to positively reduce CTEM growth rate, while R/L_{Te} serves as the primary factor responsible for high growth rates in both heating cases. As the poloidal wavelength decreases, the amplitude of the mode structure gradually decreases. Our nonlinear simulation results indicate significant suppression of ion heat transport when the zonal flow is retained, while the zonal flow expresses a stronger inhibition effect on electron heat transport in the LHW-only case. Moreover, the presence of GAM is identified in the simulations, which can play a significant regulatory role in turbulence dynamics.

Lastly, both heating scenarios feature relatively low ion temperatures. Experimentally, employing ion cyclotron resonance heating (ICRH) and neutral beam injection (NBI) can yield higher ion temperatures in principle. Consequently, the ion temperature gradient (ITG) mode may be excited, introducing an additional physics component into plasma turbulence. To comprehensively investigate instabilities under multi-wave combined heating and quantitatively compare simulations with experimental observations, more realistic gyrokinetic simulations are necessary, incorporating actual plasma profiles and equilibrium radial electric fields.

Acknowledgement

We thank Dr. Y.H. Huang and Y.F. Jin of the Institute of Plasma Physics, Chinese Academy of Sciences for providing experimental data.

Editor Hartmut Zohm thanks the referees for their advice in evaluating this article.

Funding

The work was supported by the National Natural Science Foundation of China under Grant No. 11775108.

Declaration of interests

The authors report no conflict of interest.

REFERENCES

- BONANOMI, N., MANTICA, P., SZEPEESI, G., HAWKES, N., LERCHE, E., MIGLIANO, P., PEETERS, A., SOZZI, C., TSALAS, M., VAN EESTER, D., JET CONTRIBUTORS 2015 Trapped electron mode driven electron heat transport in JET: experimental investigation and gyro-kinetic theory validation. *Nucl. Fusion* **55** (11), 113016.
- DIAMOND, P.H., ITOH, S.-I., ITOH, K. & HAHM, T.S. 2005 Zonal flows in plasma—a review. *Plasma Phys. Control Fusion* **47** (5), R35.
- DICKINSON, D., ROACH, C.M., SKIPP, J.M. & WILSON, H.R. 2014 Structure of micro-instabilities in tokamak plasmas: Stiff transport or plasma eruptions? *Phys. Plasmas* **21** (), .
- DIMITS, A.M. & LEE, W.W. 1993 Partially linearized algorithms in gyrokinetic particle simulation. *J. Comput. Phys.* **107** (2), 309–323.
- DING, S., JIAN, X., GAROFALO, A.M., YAN, Z., MCCLENAGHAN, J., GUO, W. & GRIERSON, B.A. 2019 The dominant micro-turbulence instabilities in the lower q_{95} high β_p plasmas on DIII-D and predict-first extrapolation. *Nucl. Fusion* **60** (1), 016023.
- DONG, J., CHEN, L. & ZONCA, F. 1999 Study of kinetic shear Alfvén modes driven by ion temperature gradient in tokamak plasmas. *Nucl. Fusion* **39** (8), 1041–1050.
- DUMONT, R.J. & GIRUZZI, G. 2004 Theory of synergy between electron cyclotron and lower hybrid waves. *Phys. Plasmas* **11** (7), 3449–3459.
- FIDONE, I., GIRUZZI, G., KRIVENSKI, V., MAZZUCATO, E. & ZIEBELL, L.F. 1987 Cross-effect on electron cyclotron and lower hybrid current drive in tokamak plasmas. *Nucl. Fusion* **27**, 579–587.
- GAO, Z. 2010 Plasma shaping effects on the geodesic acoustic mode in the large orbit drift width limit. *Phys. Plasmas* **17** (9), 092503.
- GAO, Z., ITOH, K., SANUKI, H. & DONG, J.Q. 2006 Multiple eigenmodes of geodesic acoustic mode in collisionless plasmas. *Phys. Plasmas* **13** (10), 100702.
- GIRUZZI, G., ARTAUD, J.F., DUMONT, R.J., IMBEAUX, F., BIBET, P., BERGER-BY, G., BOUQUEY, F., CLARY, J., DARBOS, C., EKEDAH, A., HOANG, G.T., LENNHOLM, M., MAGET, P., MAGNE, R., SÉGUI, J.L., BRUSCHI, A. & GRANUCCI, G. 2004 Synergy of electron-cyclotron and lower-hybrid current drive in steady-state plasmas. *Phys. Rev. Lett.* **93**, 255002.

- HAHM, T.S. 1988 Nonlinear gyrokinetic equations for tokamak microturbulence. *Phys. Fluids* **31** (9), 2670–2673.
- HAHM, T.S., WANG, L. & MADSEN, J. 2009 Fully electromagnetic nonlinear gyrokinetic equations for tokamak edge turbulence. *Phys. Plasmas* **16** (2), 022305.
- HORTON, W. 1999 Drift waves and transport. *Rev. Mod. Phys.* **71**, 735–778.
- LANG, J., CHEN, Y. & PARKER, S.E. 2007 Gyrokinetic δf particle simulation of trapped electron mode driven turbulence. *Phys. Plasmas* **14** (8), 082315.
- LANG, J., PARKER, S.E. & CHEN, Y. 2008 Nonlinear saturation of collisionless trapped electron mode turbulence: Zonal flows and zonal density. *Phys. Plasmas* **15** (5), 055907.
- LAO, L.L., JOHN, H.S., STAMBAUGH, R.D., KELLMAN, A.G. & PFEIFFER, W. 1985 Reconstruction of current profile parameters and plasma shapes in tokamaks. *Nucl. Fusion* **25** (11), 1611.
- LIN, Z., HAHM, T.S., LEE, W.W., TANG, W.M. & WHITE, R.B. 1998 Turbulent transport reduction by zonal flows: Massively parallel simulations. *Science* **281** (5384), 1835–1837.
- LIN, Z., NISHIMURA, Y., XIAO, Y., HOLOD, I., ZHANG, W.L. & CHEN, L. 2007 Global gyrokinetic particle simulations with kinetic electrons. *Plasma Phys. Control. Fusion* **49** (12B), B163.
- LIN, Z., TANG, W.M. & LEE, W.W. 1995 Gyrokinetic particle simulation of neoclassical transport. *Phys. Plasmas* **2** (8), 2975–2988.
- QIAN, J.P., LAO, L.L., LIU, H.Q., DING, W.X., ZENG, L., LUO, Z.P., REN, Q.L., HUANG, Y., HUANG, J., BROWER, D.L., HANADA, K., CHEN, D.L., SUN, Y.W., SHEN, B., GONG, X.Z., XIAO, B.J. & WAN, B.N. 2016 East equilibrium current profile reconstruction using polarimeter-interferometer internal measurement constraints. *Nucl. Fusion* **57** (3), 036008.
- REWOLDT, G., LIN, Z. & IDOMURA, Y. 2007 Linear comparison of gyrokinetic codes with trapped electrons. *Comput. Phys. Commun.* **177** (10), 775–780.
- RYTER, F., ANGIONI, C., DUNNE, M., FISCHER, R., KURZAN, B., LEBSCHY, A., MCDERMOTT, R.M., SUTTROP, W., TARDINI, G., VIEZZER, E., WILLENSDORFER, M., THE ASDEX UPGRADE TEAM 2019 Heat transport driven by the ion temperature gradient and electron temperature gradient instabilities in ASDEX upgrade H-modes. *Nucl. Fusion* **59** (9), 096052.
- RYTER, F., ANGIONI, C., PEETERS, A.G., LEUTERER, F., FAHRBACH, H.-U. & SUTTROP, W. 2005 Experimental study of trapped-electron-mode properties in tokamaks: threshold and stabilization by collisions. *Phys. Rev. Lett.* **95**, 085001.
- WANG, Y.M., GAO, X., LING, B.L., ZHANG, S.B., ZHANG, T., HAN, X., LIU, S.C., LIU, Z.X., LIU, Y. & TI, A. 2013 Development of the W-band density profile and fluctuation reflectometer on EAST. *Fusion Engng Des.* **88** (11), 2950–2955.
- XIAO, Y., HOLOD, I., WANG, Z., LIN, Z. & ZHANG, T. 2015 Gyrokinetic particle simulation of microturbulence for general magnetic geometry and experimental profiles. *Phys. Plasmas* **22** (2), 022516.
- XIAO, Y., HOLOD, I., ZHANG, W.L., KLASKY, S. & LIN, Z. 2010 Fluctuation characteristics and transport properties of collisionless trapped electron mode turbulence. *Phys. Plasmas* **17** (2), 022302.
- XIE, H.S., XIAO, Y. & LIN, Z. 2017 New paradigm for turbulent transport across a steep gradient in toroidal plasmas. *Phys. Rev. Lett.* **118**, 095001.
- ZHAO, C. & XIAO, Y. 2018 Nonlinear gyrokinetic particle simulation of dissipative trapped electron mode. *Phys. Plasmas* **25** (10), 102303.
- ZHENG, S.Y., ZHANG, D.B., XUE, E.B., YU, L.M., ZHANG, X.M., HUANG, J., XIAO, Y., WU, M.Q., GONG, X.Z., EAST TEAM 2022 Study of turbulence in the high β_p discharge using only RF heating on EAST. *Plasma Phys. Control Fusion* **64** (4), 045017.